Numerical analyses of energy balance and installation mechanisms of large-diameter tapered monopiles by impact driving

Chen, Fuquan; Liu, Liyang ; Lai, Fengwen; Gavin, Kenneth; Flynn, Kevin N. ; Li, Yida

DOI
10.1016/j.oceaneng.2022.113017

Publication date
2022

Document Version
Final published version

Published in
Ocean Engineering

Citation (APA)
Chen, F., Liu, L., Lai, F., Gavin, K., Flynn, K. N., & Li, Y. (2022). Numerical analyses of energy balance and installation mechanisms of large-diameter tapered monopiles by impact driving. *Ocean Engineering*, *266*(Part 4), Article 113017. https://doi.org/10.1016/j.oceaneng.2022.113017

Ocean Engineering 266 (2022) 113017

Contents lists available at ScienceDirect

Ocean Engineering

journal homepage: www.elsevier.com/locate/oceaneng

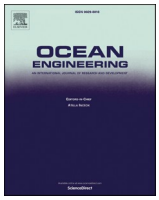

Numerical analyses of energy balance and installation mechanisms of large-diameter tapered monopiles by impact driving

Fuquan Chen [a], Liyang Liu [a], Fengwen Lai [b,c,*], Kenneth Gavin [c], Kevin N. Flynn [d], Yida Li [a]

[a] College of Civil Engineering, Fuzhou University, Fuzhou, 350116, PR China
[b] Institute of Geotechnical Engineering, Southeast University, Nanjing, 211189, PR China
[c] Faculty of Civil Engineering and Geosciences, Delft University of Technology, 2628 CN, Delft, the Netherlands
[d] Brazil Piling & Foundations, Dunboyne, Ireland

ARTICLE INFO

Keywords:
Finite-element modeling
Piles & piling
Impact driving
Offshore wind turbines
Energy balance
Installation mechanism
Drivability performance

ABSTRACT

Large-diameter monopiles are widely used as the foundation to support offshore wind turbines (OWTs) in shallow coastal waters. The benefits of small-to-medium diameter tapered piles have been reported in the past. The potential use of large-diameter tapered monopiles installed by impact driving to support OWTs is thus presented, and then comparatively assessed by numerical analyses in terms of energy balance and installation mechanisms. A three-dimensional large deformation finite element (3D-LDFE) model of monopiles driven in clay was developed using a Coupled Eulerian-Lagrangian (CEL) approach. An advanced user-defined hypoplasticity clay (HC) model was employed to model undrained kaolin clay, featuring nonlinear behavior from small strain to large strain. The force-time curve defined by the operating data of a state-of-the-art hammer in the offshore industry was inputted to explicitly model impact driving. Better agreement between the measured and the simulated results was observed to validate the accuracy of the numerical model. The numerical results obtained give greater confidence to the future use of large diameter tapered monopiles for OWTs.

1. Introduction

Offshore wind energy provides a key component of the renewable and sustainable energy mix. Offshore developments are gaining traction worldwide, with a rapid expansion of offshore wind turbines (OWTs) being constructed in recent years. Monopiles are currently the preferred foundation solution for supporting OWTs in shallow coastal water (Byrne et al., 2020a, 2020b; Chortis et al., 2020; Zdravkovic et al., 2020; Fan et al., 2021; Sunday and Brennan, 2021), benefiting from the ease of fabrication and installation offshore. The bearing capacity characteristics of monopile have been required to be improved as the cumulative power of OWT increases, leading to an increase in monopile diameter larger than 10m with most OWTs being installed using impact driving, see Fig. 1. The potential of piles with a tapered section (known as tapered or semi-tapered piles) has been confirmed through both extensive experimental observations and theoretical developments (Kodikara and Moore, 1993; Kurian and Srinivas, 1995; El Naggar and Wei, 1999; Kodikara et al., 2006; Tavasoli and Ghazavi, 2019, 2020), from a viewpoint of bearing capacity. Typically, the tapered pile is defined as a pile that has a taper over the full length or in the embedded section, while the semi-tapered pile is known as a pile that has only part of its section tapered (usually the part which is submerged). There has been a lot of evidence showing that the geometric configuration of monopiles can be optimized toward the practical design from a straight-sided cylindrical shape to a fully or partly conical type. In this context, we first present a study of large diameter tapered monopiles potentially used for supporting OWTs.

Reliable pile driving predictions and a thorough understanding of the factors that influence the process are indispensable for the development of an accurate practical design methodology, also for optimal hammer selection. Numerous researchers have investigated the installation effects of tapered piles. Sakr and El Naggar (2003) first performed centrifuge tests to model tapered and cylindrical piles driven into loose sand, the observed taper effect was further compared with the analytical solutions using the cavity expansion method (CEM). They reported that the axial load capacity of tapered piles would be higher than that of cylindrical piles with equal average diameter, and the difference increased with increasing tapered angle. Kodikara et al. (2006) presented a two-dimensional (2D) numerical evaluation of the skin resistance of bored tapered piles in mudstone to assess their feasibility against cylindrical piles, the effects of taper angle, mean pile diameter,

* Corresponding author. Institute of Geotechnical Engineering, Southeast University, PR China.
E-mail address: laifengwen@163.com (F. Lai).

https://doi.org/10.1016/j.oceaneng.2022.113017
Received 1 February 2022; Received in revised form 1 October 2022; Accepted 25 October 2022
Available online 9 November 2022

List of notations

A Area of pile head A_g Parameter controlling the stiffness magnitude c Area of pile head A_g Parameter controlling the stiffness magnitude c Soil cohesion
D Inner diameter of single pile foundation D_c Inner diameter of single pile foundation D_c Diameters of equal diameter monopile
D_t Diameters of monopile top
D_b Diameters of monopile bottom
D_{eq} Equivalent diameter of monopiles
D_r Reference rate
e Void ratio
e_0 Initial void ratio E Young's modulus E_C Initial void ratio E Young's modulus E_C Energy dissipated by time-dependent deformation
E_F Energy dissipated by contact force
E_I Internal energy
E_P Energy dissipated by plastic strain
E_s Young's modulus
E_S Applied elastic strain energy
E_V Energy dissipated by viscous effects
E_W Cumulative driving energy delivered by hammer impact on the pile head
E_{WC} Maximum cumulative driving energy of MP-C
$E_{Balance}$ Constant representing energy balance E_K Instantaneous kinetic energy of the pile-soil system f_{max} Maximum instantaneous impact driving force f_s Constant representing energy balance E_K Instantaneous kinetic energy of the pile-soil system f_{max} Maximum instantaneous impact driving force f_s Unit sleeve friction resistance
F Driving force varies with time under 1g condition F_b Base resistance F_c Total imposed driving load F_s Driving force varies with time under 1g condition F_b Base resistance F_c Total imposed driving load F_s Skin resistance
F_t Total resistance g Gravitational acceleration G_0 Total resistance g Gravitational acceleration G_0 Small-strain stiffness
h Dropping height of ram h_0 Height of void layer h_v Dropping height of ram h_0 Height of void layer h_v Hammer penetration depth
H Penetration depth I_v Viscosity index k Penetration depth I_v Viscosity index k Permeability coefficient
K_0 Coefficient of earth pressure at rest L Length of monopiles L_c & L_t Coefficient of earth pressure at rest L Length of monopiles L_c & L_t Length of various sections for monopiles with various geometries
m Quality of ram
$\boldsymbol{m}_{pile}$ Quality of pile body
m_{rat} Parameter controlling the initial shear modulus
$\boldsymbol{m}_{soil}$ Mass density of soil particles
M Quality of hammer N Parameter controlling the slope of the isotropic unloading line N_{hammer} & N_{SPT} Quality of hammer N Parameter controlling the slope of the isotropic unloading line N_{hammer} & N_{SPT} Blow counts of hammer and SPT
N_{kt} Cone factor
n_g Curvature of the $G_0 - p$ line
p_r Reference stress q_{max} Maximum uniform load q_c Reference stress q_{max} Maximum uniform load q_c Measured cone resistance
R Initial size of the elastic range S Initial size of the elastic range S Radial distance
s_u Undrained shear strength
t Wall thickness
t_c & t_t Wall thickness of various sections for monopiles with various geometries
u_2 Pore pressure measured behind cone
v Falling speed of Ram
v_{hammer} Velocity generated from the motion of a free falling mass $\boldsymbol{x}_{pile}$ Velocity generated from the motion of a free falling mass $\boldsymbol{x}_{pile}$ Monopile velocity history
$\boldsymbol{x}_{soil}$ Relative velocity of soil particles
z_s Buried depth of soil OCR^+ Buried depth of soil OCR^+ Overconsolidation ratio
α Frictional coefficient of pile-soil interface
β Taper angle
β_r & χ Parameter controlling the rate of degradation of the stiffness with strain
γ Unit weight
γ_{sat} Saturated unit weight
$\dot{\boldsymbol{\varepsilon}}$ Composited strain rate
$\dot{\boldsymbol{\varepsilon}}^{cr}$ Creep strain rate
$\dot{\boldsymbol{\varepsilon}}^{el}$ Elastic strain rate
$\dot{\boldsymbol{\varepsilon}}^{f}$ Relative strain rate between pile body and soil particles around
$\dot{\boldsymbol{\varepsilon}}^{pl}$ Plastic strain rate
κ^* Parameter controlling the position of the isotropic normal compression line λ^* Parameter controlling the slope of the isotropic normal compression line μ Parameter controlling the position of the isotropic normal compression line λ^* Parameter controlling the slope of the isotropic normal compression line μ Poisson's ratio
ν Parameter controlling the shear modulus ξ Parameter controlling the shear modulus ξ Damping ratio
ρ Density
$\boldsymbol{\sigma}^f$ Interface adhesion under undrained condition
$\boldsymbol{\sigma}^v$ Viscous stresses
σ_r Radial stresses
φ Peak friction angle
φ_c' Critical state friction angle $\mathbf{L}$ Critical state friction angle $\mathbf{L}$ Fourth-order tensor
$\mathbf{N}$ Second-order tensor $\overrightarrow{\boldsymbol{\delta}}$ Represents the direction of inter-granular strain $\mathring{\boldsymbol{\delta}}$ Second-order tensor $\overrightarrow{\boldsymbol{\delta}}$ Represents the direction of inter-granular strain $\mathring{\boldsymbol{\delta}}$ Equation of inter-granular strain
$\mathbf{D}$ & $\mathring{\mathbf{T}}$ Jaumann's strain-rate tensor and stress-rate tensor
$\mathbf{D}^{vis}$ Viscous strain rate

and pile length was taken into consideration. It was numerically confirmed again that the use of taper angle can provide a higher axial load capacity in comparison to cylindrical piles. Ghazavi et al. (2012) carried out three-dimensional (3D) numerical modeling of the installation of tapered piles in clayey soil, and presented that the displacements of pile toe and tip increase with increasing the taper angle, resulting in the improvement of the pile driving efficiency. The driving performance was also theoretically evaluated by Sormeie and Ghazavi (2018) using CEM combined with wave equation analyses. The results show that tapered piles are driven easier than cylindrical piles with the same length and volume. As such, the numerical and analytical evidence both confirmed that tapered and semi-tapered piles can provide better drivability performances than cylindrical piles. Tavasoli and Ghazavi (2018); Tavasoli and Ghazavi (2019); Tavasoli and Ghazavi (2020) subsequently conducted a series of numerical and experimental investigations into drivability performances of tapered piles. The emphasis

was placed on the establishment of a correlation between pile shapes and hammer below counts. Tapering the pile was proven to efficiently decrease the cumulative hammer blow counts. For small-to-medium diameter pile, the use of tapered piles not only reduce energy consumption by at least 25%, the pile driving efficiency significantly increases.

The aforementioned studies mainly focused on the drivability performance of small-to-medium diameter tapered piles in the ground. The paper first presents the concept of large-diameter tapered OWT monopiles. The drivability of such monopiles with a tapered section is, therefore, comparatively explored against cylindrical monopiles. The energy balance analyses and associated installation mechanisms during impact driving are necessary for optimal hammer selection. For such purposes, field testing is typically consuming a lot of resources (material, equipment and manpower), and is hence very expensive. Although laboratory tests can provide a better understanding of installation mechanisms of piles on a reduced scale, they are often limited for large diameter long piles under 1g condition. Moreover, energy balance analyses are difficult to perform through field observations and laboratory tests. The widely-accepted numerical modeling technique, known as finite element method (FEM) for continuous medium or discrete element method (DEM) for granular medium, is likely a preferred option to study the large deformation problem related to the installation mechanisms and the energy balance in the system. Correspondingly, the Coupled-Eulerian-Lagrangian (CEL) approach is a powerful FEM tool to numerically simulate the installation process of large diameter monopiles in clays.

It is not the purpose of this study to provide a design procedure for monopiles, but it is a fundamental study to explore the use potential of large diameter tapered monopiles by impact driving in the offshore industry. In what follows, the driving performances of various monopiles (tapered/semi-tapered/cylindrical piles) are comparatively assessed in terms of energy exchange and installation mechanisms. An advanced user-defined hypoplasticity clay (HC) model is first employed to simulate the undrained kaolin clays. The whole installation process of various monopiles in clays is modeled using the Coupled-Eulerian-Lagrangian (CEL) approach. The energy balance analyses during the whole installation process and each hammer blow are presented, respectively. The installation mechanisms associated with hammer blow counts, penetration resistances, and radial stresses are finally investigated.

2. Numerical modeling details

2.1. CEL approach for large deformation problems

3D large deformation finite-element (LDFE) problems have been widely studied using the Coupled-Eulerian-Lagrangian approach incorporated in the commercial finite element program ABAQUS/Explicit. The feasibility and applicability of the CEL approach have been also proven for various geotechnical penetration problems such as the installations of piles (Fan et al., 2021; Li et al., 2021), caissons (Lai et al., 2020, 2021, 2022a, 2022b; Harireche et al., 2021), spudcans (Li et al., 2018) and CPTs (Wang et al., 2019; Gavin et al., 2021), etc.

CEL approach possesses the advantages both of Lagrangian and Eulerian formulations. The Lagrangian formulation yields the deformable mesh that moves in sync with materials, implying that the displacement of the continuum can be expressed as a function of time and material coordinates. The geo-structures (e.g. piles) are typically discretized as Lagrangian elements Nonetheless, for Eulerian formulation, the displacement of the continuum is characterized by a function of time and spatial coordinates. As such, the materials and meshes are mutually independent, which enables the meshes to avoid distortion, hence being capable of ensuring computational stability. The Eulerian element is always used to model soils with large deformation. The definition of Eulerian volume fraction (EVF) representing the portion of that element filled with a specified material is introduced to track the

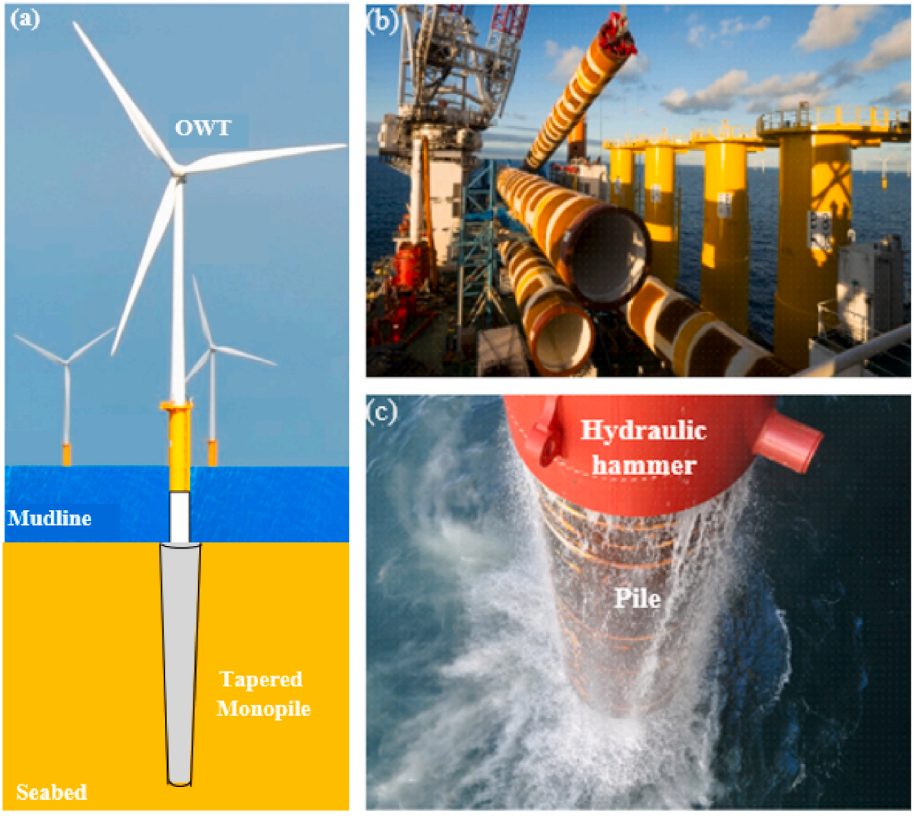

Fig. 1. Offshore wind turbine founded on monopiles: (a) Structural components(Charlton and Rouainia, 2020); (b) Construction site (https://iqip.com) (c) Hammer impacting process (https://iqip.com).

material flow. EVF = 1 indicates that meshes are fully filled with materials, EVF < 1 means that the meshes are partially occupied by materials, and the rest are filled by void elements. Hence EVF = 0 represents that no material is filled in the meshes. More details of the CEL approach can be found in (Lai et al., 2020) and omitted here.

2.2. Force-time input

Hydrohammer® S-4000 (free access on https://www.ihciqip.com), a state-of-the-art hydraulic impact hammer, is selected for driving steel large diameter offshore piles in this study. The detailed composition of the equipment is sketched in Fig. 2(a). The operating principle of such a hydraulic hammer is presented in Fig. 2(b), all the accessories are simplified as a steel holder and energy accumulator to transfer the dead weight and transport the hammer ram with deadweight $m = 200$ tons. The cycle operation begins with the lifting phase of the ram, denoted as *Phase 1*. In this phase with the duration $t_1 \approx 2$ s, the hammer ram can be lifted at a specific height $h = 2$ m and prepared for the next blow. In the next phase (here defined as *Phase 2*), the pile head and hammer ram are fully in contact with the impact driving duration $t_2 \approx 0.02$ seconds (Vantomme et al., 2019). The total imposed driving load on the pile head can be calculated as:

$$F_c = F(t) + Mg \tag{1}$$

where $F(t)$ is the impact driving force varies with time under 1g condition, Mg is the total deadweight of the hydraulic hammer with ram and mounting on the pile head. Constant load$Mg = 430$ tons, documented on the above website, can be defined as the self-weight of the whole equipment.

Fig. 2(c) shows the variation of impact driving force with time following an ideal sinusoidal function. Therefore, we can present the following functional relationship:

$$F(t) = f_{\max} \sin\left(\frac{\pi t}{t_2}\right) \tag{2}$$

$$\int_x^{x+t_2} F(t)dt = -f_{\max}\frac{t_2}{\pi}\cos\frac{\pi t}{t_2}\Big|_0^{t_2} = f_{\max}\frac{2t_2}{\pi} \tag{3}$$

where $f_{\max}$ is the maximum instantaneous impact driving force.

Under the gravity, considering the kinetic energy formula, we have

$$\int_0^{t_2} F(t)dt = mv_{hammer} = m\sqrt{2gh} \tag{4}$$

where v_{hammer} is the velocity generated from the motion of a free-falling mass.

Combining Eq. (3) and Eq. (4), we obtain

$$f_{\max}\frac{2t_2}{\pi} = m\sqrt{2gh} \rightarrow f_{\max} = \frac{\pi m\sqrt{2gh}}{2t_2} \tag{5}$$

For Hydrohammer® S-4000, we can transfer input parameters as the driving force from Eq. (5), as below:

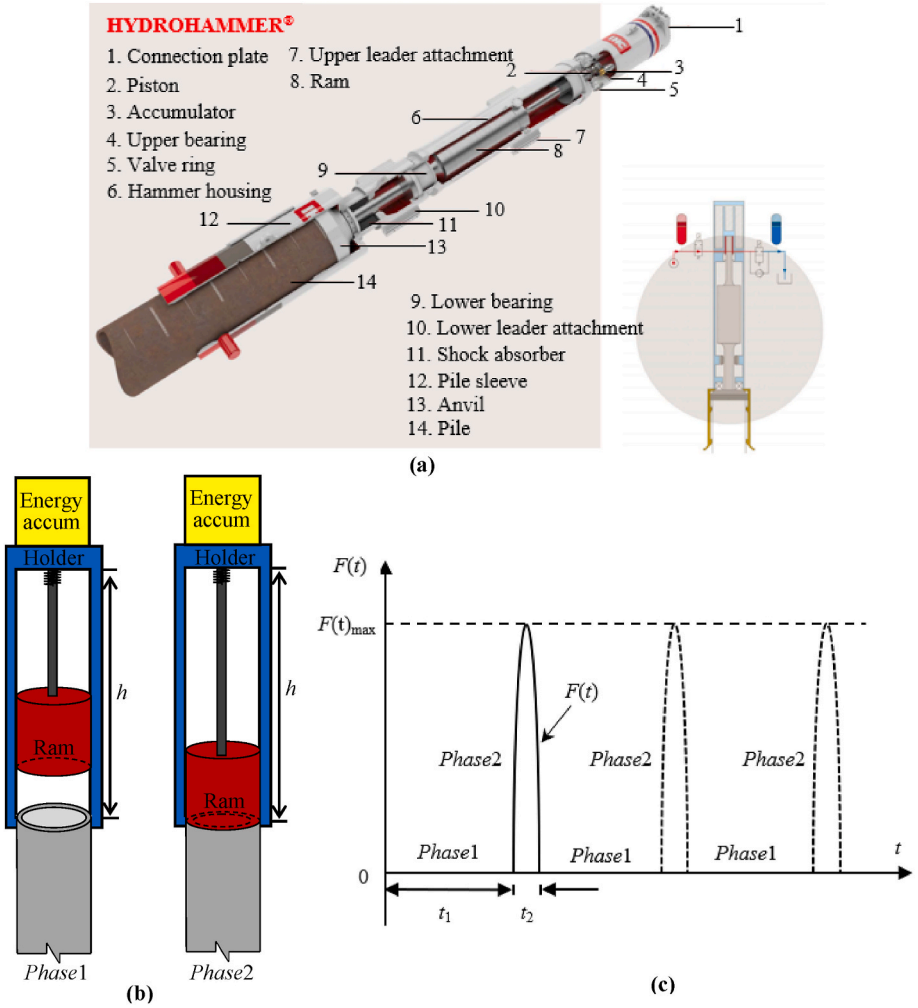

Fig. 2. Hydraulic hammer simulated in the numerical model: (a) details of Hydrohammer® S-4000; (b) operating principle and (c) force-time curve.

$$f_{\max}=\frac{\pi m\sqrt{2gh}}{2t_2}=\frac{\pi\times 200\times\sqrt{2\times 9.81\times 2}}{2\times 0.02}=98347.69\ \text{kN} \tag{6}$$

Postulating OWT monopile has a wall thickness of 0.1 m and an internal diameter of 10.0 m (as mentioned below), the maximum uniform load can be obtained:

$$q_{\max}=\frac{f_{\max}}{A}=\frac{4\times 98347.69}{\pi\times\left(10.2^2-10^2\right)} \tag{7}$$

In the model, we only input a force-time curve shown in Fig. 2(c) into ABAQUS/Explicit to numerically define the hammer impact.

Note that the interval t_1 means a long duration for a hammer blow as the hammer ram has to be lifted and prepared for the next blow. In the model, this duration of around 30 min is computationally expensive. Such intervals need to be reduced to a lower computational cost. However, the blow intervals are not placed overly closely, which might result in a significantly varied piling acceleration. That is, the next blow should be imposed at a time that can ensure the pile is in mechanical equilibrium. The interval of 0.18 s can be assumed to be large enough to avoid overlapping in the piling acceleration (Daryaei et al., 2020).

2.3. Geometric configuration and numerical model generation

To examine the effect of the geometric configuration of tapered monopiles on drivability performance, four different geometries are considered in the numerical model, as shown in Fig. 3(a)-3(d). A standard straight-sided cylindrical shape, MP-C, and a fully tapered, MP-T are considered. In addition, two partially-tapered monopiles, MP-CT and MP-TC (Tavasoli and Ghazavi, 2020), are analyzed. MP-CT is composed of an upper cylindrical part with a length of 30m and a lower tapered part with a length of 30m. MP-TC has an upper tapered part connected by a cylindrical part. It is postulated that these monopiles have equal material volume and penetration depth. In the model, the total penetration depth L for four monopiles is 60m, the diameter is 10m, the wall thickness is $t = 1\%D$ and a taper angle of 2° is assumed. The other geometric configurations can be calculated and summarized in Table 1.

Based on the geometric configurations an 8°-slice numerical model can be considered in Fig. 4, for the sake of reducing the computational cost. The homogeneous kaolin clay was chosen as seabed soil with undrained installation conditions assumed. The monopiles were made of ST37 steel (ASTM-A252, 2010). An advanced user-defined HC model was programmed to model undrained clay and rigid body behavior is assumed for the monopile (Daryaei et al., 2020; Lai et al., 2020; Wang et al., 2020; Soleimani and Weienfels, 2021). The principal advantage to

Table 1
Geometric configurations of various monopiles.

Pile type	Total pile length (mm)	Tapered angle β (°)	Diameter D (mm)		Pile thickness (mm)
			Top (D_t)	Toe (D_b)	
MP-C	$L_c = 6000$	–	1000	1000	$t_c = 100$
MP-T	$L_t = 6000$	2	1229	810	$t_t = 1\%D_t$
MP-CT	$L_t + L_c = 3000 + 3000$	2	1072	862	$t_c = 107, t_t = 1\%D_t$
MP-TC	$L_t + L_c = 3000 + 3000$	2	1176	966	$t_c = 97, t_t = 1\%D_t$

simulating monopiles with rigid bodies rather than deformable finite elements is computational efficiency and numerical stability (strongly oscillating results in elastic body). It should be, however, noted that the assumption of rigidity may not precisely predict the wave transmission within the monopile itself, which somehow causes a deviation to from reality for energy exchange as the compression wave cannot be well captured in a rigid body. Moreover, rigid body assumption means the hammer blow must mobilize the full mass of the pile at the same time, rather than progressively as the force wave moves down the pile (elastic body). As such, the use of a rigid body may underestimate the penetration resistance of monopiles. In this paper, emphasis is put on the installation mechanisms rather than a design procedure, so the deviation arising here can be acceptable.

The soil domain was extended to 24 radii, R radially, and $2L$ vertically to eliminate the boundary effect during the piling. A 5-m-thickness (i.e. $H/12$) void layer was placed above the intact clay surface, allowing the clay to heave by flowing into the empty Eulerian elements. Both the void and the clay layers were discretized as EC3D8R elements, while the monopile was simulated using C3D8R elements. The velocity as a variable was used for controlling the initial boundary conditions of the axisymmetric model. Symmetric boundary conditions are fixed on the two lateral planes (t-direction) by prescribing zero flow velocity normal to these two planes. The model base with fully restraint against the flow is defined. For the far-field boundary (curved face, r-direction), radial flows are constrained. During the penetration, monopile is fully constrained other than z-direction under impact driving.

2.4. Mesh convergence studies

Mesh convergence studies were conducted to guarantee that the FE meshes are sufficiently fine to attain accurate results. Fine meshes around the monopiles also enable the pile-soil interface to maintain computational stability. A fine zone with $3R \times 2L$ was first created with

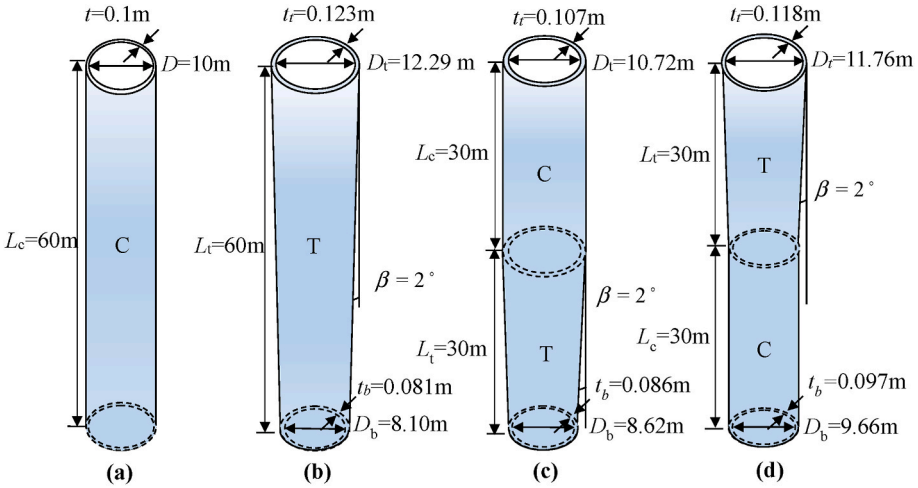

Fig. 3. Geometric configurations of monopiles with various geometries: (a) MP-C; (b) MP-T; (c) MP-CT and (d) MP-TC.

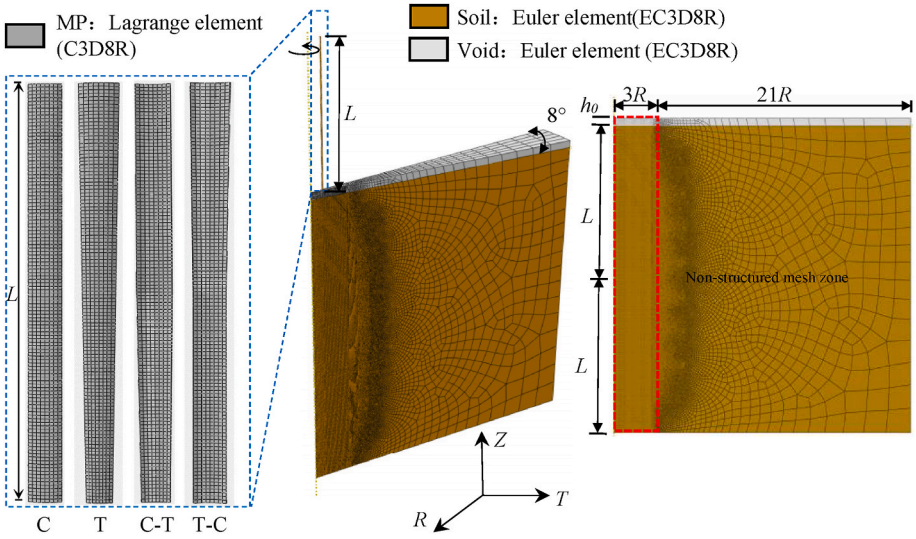

Fig. 4. Numerical model and finite-element mesh strategy.

structured meshes and the rest zone that has lesser influence on the results possesses the non-structured meshes (Fig. 4). The mesh density progressively increases from *Mesh 1* to *Mesh 3* with *Mesh 1* ($2t \times t$) being the coarsest, followed by *Mesh 2* ($t \times 0.33t$), and *Mesh 3* ($0.5t \times 0.025t$) being the finest. Fig. 5 presents a mesh convergence study showing the relationship between hammer blow counts (N_{hammer}) and penetration depth (H/L), the comparison of computation time is also given. It follows that *Mesh 2* and *Mesh 3* yield the approximate $N_{hammer} - H/L$ curves, nonetheless the computation time of *Mesh 2* is around four times that of *Mesh 3* (98.41 *h* and 364.40 *h*). Therefore, *Mesh 2* is chosen for the following numerical simulation to balance both accuracy and efficiency of the simulation.

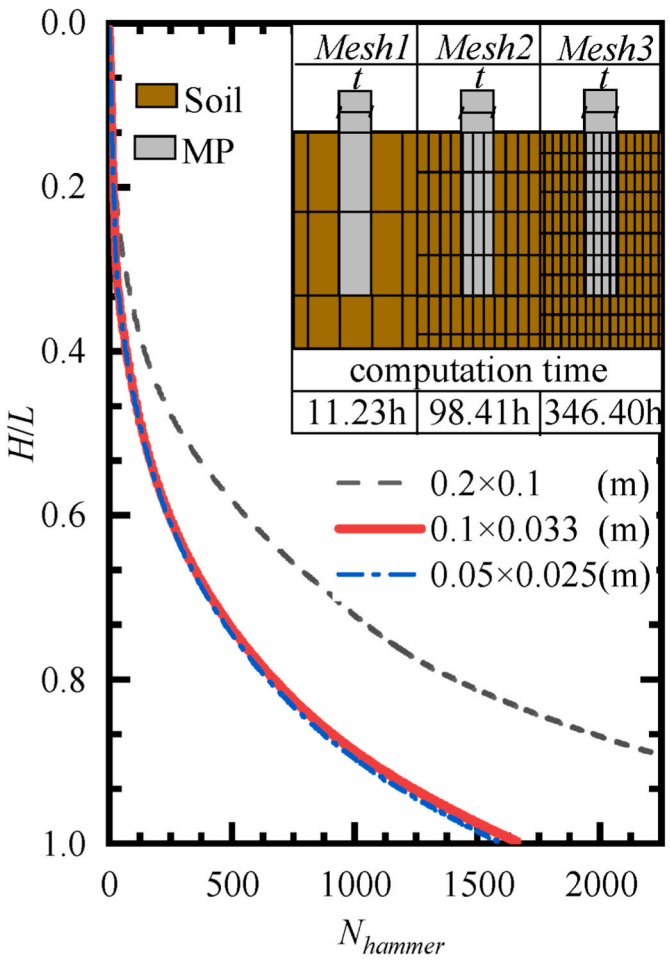

Fig. 5. Hammer blow counts-penetration depth curves for three different mesh densities.

2.5. Constitutive law and material parameters

Impact driving of piles is a cyclic loading-unloading process, leading to an extremely complex stress-strain relationship. During installation, degradation in clay stiffness from very small to large strain and the incrementally non-linear behaviors of clay and unloading-reloading can be observed. Hypoplaticity (Masin, 2014; Stutz et al., 2017; Kadlicek and Masin, 2020), is introduced to realistically describe the clay behaviors from medium to large strain. The concept of inter-granular strain is further presented to consider small-strain behavior. In hypoplaticity clay (HC) model, the yield surface and plastic potential do not have to be captured, which is entirely different from the conventional elastoplastic model. The elasticity and plasticity of clay are also not distinguished owing to the use of strain rate. The general constitutive law can be mathematically described as (Mašín, 2019):

$$\mathring{\mathbf{T}} = f_s(\mathbf{L} : \mathbf{D} + f_d \mathbf{N}\|\mathbf{D}\|) \tag{8}$$

where $\mathring{\mathbf{T}}$ and $\mathbf{D}$ are Jaumann's stress-rate tensor and strain-rate tensor, soil strength and general asymptotic responses are controlled by a fourth-order tensor $\mathbf{L}$ and a second-order tensor $\mathbf{N}$.

The equation of inter-granular strain can be written as (Mašín, 2019):

$$\mathring{\boldsymbol{\delta}} = \begin{cases} \left(\mathbf{I} - \vec{\boldsymbol{\delta}} \otimes \vec{\boldsymbol{\delta}} \rho^{\beta}\right) : \mathbf{D}\,\vec{\boldsymbol{\delta}} : \mathbf{D} > 0 \\ \mathbf{D}\,\vec{\boldsymbol{\delta}} : \mathbf{D} \le 0 \end{cases} \tag{9}$$

where $\mathring{\boldsymbol{\delta}}$ represents the direction of inter-granular strain, β_r controls the slope of the rate curve inter-granular strain tensor.

Masin (2014) suggested that the small-strain stiffness G_0 can be described as:

$$G_0 = p_r A_g \left(\frac{p}{p_r}\right)^{n_g} \tag{10}$$

where, p and p_r are the mean and reference stress, respectively; A_g and n_g are the parameters controlling the stiffness magnitude and curvature of the $G_0 - p$ line, respectively.

The viscous (strain rate) effects during shearing are is very fundamental, of course also introduced in the HC model. The expression reflecting the viscosity of the HC model can be written as (Mašín, 2019):

$$\mathring{\mathbf{T}} = f_s \mathbf{L} : \left(\mathbf{D} - \mathbf{D}^{\mathbf{vis}}\right) \tag{11}$$

where $\mathbf{D}^{\mathbf{vis}}$ is the viscous strain rate:

$$\mathbf{D}^{\mathbf{vis}} = D_r \vec{\mathbf{m}} \left(\frac{1}{OCR^{+}}\right)^{1/I_v} \tag{12}$$

where D_r is the reference rate, I_v is the viscosity index and OCR^{+} is the overconsolidation ratio. Herein, the normal consolidation is considered (i.e. OCR = 1).

The material parameters of the HC model for the Kaolin Clay are summarized in detail and calibrated by Lai et al. (2020), and further given in Table 2. HC model has five basic parameters of HC model ($\varphi_c^{'}$, λ^*, N, κ^* andν), and all the associated definitions of parameters used have been given in Table 2. The model requires another set of six parameters capturing the small-strain behavior (β_r, χ, n_g, A_g, m_{rat} and R). An additional set of four physical parameters are also required as the input (e_0, γ_{sat}, k_0 and$k$). It should be emphasized that four out of the 11 parameters for kaolin clay have been extensively reported ($\varphi_c^{'}$, λ^*, N andκ^*). The other seven model parameters controlling soil stiffness from small to large strain have been calibrated in previous experimental studies.

A linear-elastic model was used to model the monopiles. Table 3 lists the associated model parameters (ASTM-A252, 2010). The interaction between the monopile and the clay was modeled using a general contact algorithm that is based on a penalty contact method. The pile-soil interface was thus modeled as frictional contact using this algorithm and specifying a reduction coefficient (adhesion factor for clay). The value of reduction coefficient α of the pile-soil interface is typically between 0.2–0.4 (Pucker and Grabe, 2012; Lai et al., 2020). A lower bound of 0.2 was adopted in this simulation to do a conservative estimation as the CEL approach implemented in Abaqus/Explicit does not allow us to introduce a user-defined contact algorithm where the friction fatigue can be modeled. Moreover, the impact driving monopile is a dynamic process in essence. Rayleigh stiffness ratio damping was thus introduced in the model to lower the vibration wave transmission to the far-field boundary. A damping ratio ($\xi = 0.03$) of the viscous materials can be inputted into the model (Ekanayake et al., 2013).

Table 2
Model parameters of kaolin clays adopted in 3D LDFE analyses (Lai et al., 2021).

Category	Description	Symbol (Unit)	Value
Basic parameters	Critical state friction angle	φ_c (°)	27.5
	Parameter controlling the slope of the isotropic normal compression line in the $\ln(1+e) - \ln p$ plane	λ^*	0.065
	Parameter controlling the slope of the isotropic unloading line in the $\ln(1+e) - \ln p$ plane	N	0.918
	Parameter controlling the position of the isotropic normal compression line in the $\ln(1+e) - \ln p$ plane	κ^*	0.01
	Parameter controlling the shear modulus	ν	0.35
Intergranular strain concept parameters	Parameter controlling the rate of degradation of the stiffness with strain	β_r	0.1
	Parameter controlling the rate of degradation of the stiffness with strain	χ	0.7
	Curvature of the $G_0 - p$ line(G_0 is shear modulus)	n_g	0.5
	Parameter controlling the stiffness magnitude	A_g	5300
	Ratio of parameter m_T controlling the initial shear modulus	m_{rat}	0.7
	Initial size of the elastic range	R	1e-5
Physical parameters	Initial void ratio	e_0	1.15
	Saturated unit weight of soil	γ_{sat} (kN/m^3)	17.4
	Coefficient of earth pressure at rest	K_0	0.54
	Permeability	k (m/s)	1e-9

Table 3
Model parameters of steel monopile.

Description	Symbol	Value	Unit	Reference
Young's modulus	E	210	Gpa	Data from (ASTM-A252, 2010)
Poisson's ratio	μ	0.16	–	
Density	ρ	7.85	kg/m^3	

3. Validation

The developed numerical model was validated, in terms of hammer blow count with installation depth, against field observations conducted in Tilbury, UK. On the site, two driven cast-in-situ (DCIS) piles with a diameter of 610 mm, denoted as Pile-SE6 and Pile-SE8, were installed using a hydraulic hammer. The lengths of the piles are 14.75m and 14.80m, respectively. The hammer type was Junttan HHK5A, of which operational details were reported by Flynn and McCabe (2019). The soil classification and characterization were based on Piezocone Tests (CPTu). The CPTu data indicates that the soil profile includes 3m of made ground overlying a thick layer of soft clay (between 3m deep and 14m deep), followed by medium dense sand (Fig. 6).

For simplification, the sand layer at the bottom is neglected in the numerical model as the piles are only partially embedded in this layer (around 0.8m). On this account, we only calibrated the model parameters of the top two soil layers using the CPTu data. Undrained shear strengths for made ground and soft clays are determined from piezocone tests using a cone factor N_{kt} of 11.6 calibrated using shear vane tests carried out by Skempton (1953) at Tilbury, UK, which is presented in Fig. 6 (e). As such, a linearly increasing undrained strength profile of soft clays with depth can be approximated as

$$s_u = 1.81z + 7.83 \tag{13}$$

An empirical relationship of $E_u = 350S_u$ is further adopted to estimate the undrained Young's modulus (Lunne et al., 2002) such that the so-called Gibson's foundation soil is approximately modeled (Daryaei et al., 2020). Additionally, the mean cone penetration resistance of a thinner layer of made ground is used to estimate the corresponding undrained strength and Young's modulus. Detailed parameters are presented in Table 4. In the model, to consider the potential energy losses during hammer impacting due to some avoidable factors such as noise and heat, a lower bound value of hammer efficiency of 0.8 suggested by Rausche and Klesney (2007) is selected to calculate the total driving energy E_w, which can be achieved by defining the force-time curve with $f_{\max} = 1523.60$ kN, as mentioned above.

Fig. 7 shows comparisons of hammer blow count (N) between the numerical and the observed results with the normalized installation depth for Pile-SE6 and Pile-SE8. It is clear that the numerical results obtain a better agreement with the observed results. The reasons why the slight overestimation of N_{hammer} value in soft clays is found can be given as follows: (a) the hammer efficiency is over-estimated, and the realistic driving energy may have been more than 80%; and (b) a direct use of reduction coefficient to estimate the strength of pile-soil interface such that softening effect-enabled residual value was not realistically considered here. In all, the developed numerical model is capable of providing an acceptable estimation for the hammer blow count.

4. Energy balance analyses

The hammer energy needs to cover the required driving energy to

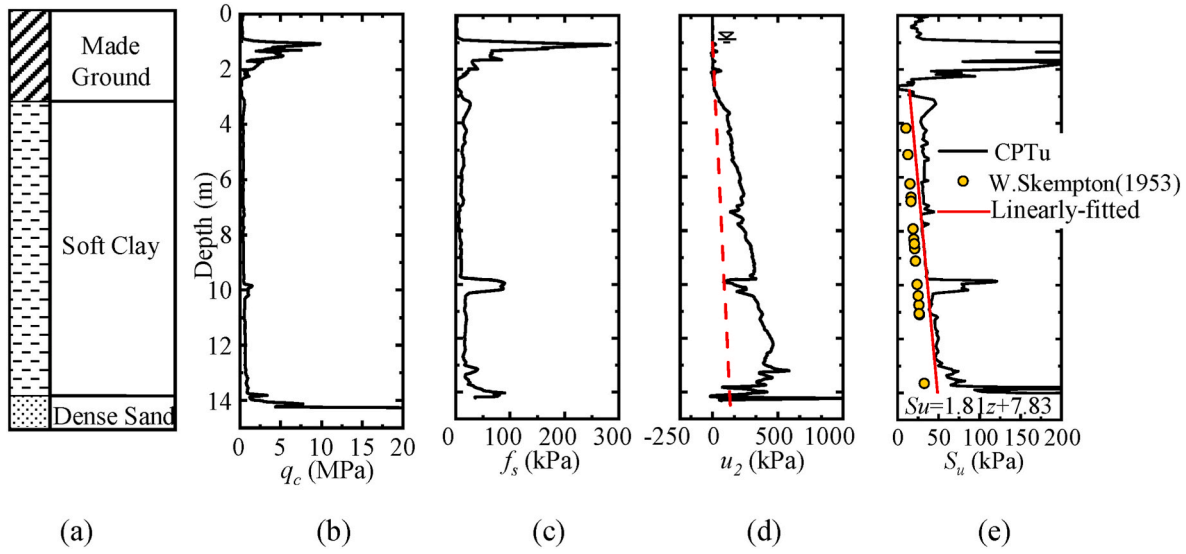

Fig. 6. The CPTu soundings and interpretation results at Tilbury site: (a) soil profile; (b) corrected cone resistance; (c) sleeve friction; (d) pore water pressure; (e) interpreted undrained strength.

Table 4
Soil parameters used in the numerical model for field-test.

Parameter	Top-level (m)	Unit weight γ (kN/m^3)	Undrained strength s_u (kPa)	Young's modulus E (Mpa)	Posson's ratio ν (−)
Made ground	0	20.5	196	68.6	0.495
Clay	3	19.63	13.3–33.2	4.65–11.62[a]	0.495

Note: [a] $E_u = 350 s_u$

overcome the soil resistance, wall-soil interface contact, and energy losses resulting from the water column, heat, and noise. The proportion of energy losses during impact driving can reach around 5.0–10.0% for large diameter offshore monopiles (Vantomme et al., 2019). This work mainly focuses on the hammer energy dissipation process in the soil, the associated energy losses are thus not involved as the water domain needs to be modeled using the complex acoustic elements, also the effect of noise is not considered in the numerical model (Flynn and McCabe, 2019). This section will provide insights into the dissipation and exchange of different energy terms during a hammer blow and during the whole process.

4.1. Cumulative driving energy

The cumulative driving energy delivered from hammer energy on the pile head for four monopile geometries considered (here denoted as the work done, E_W), is plotted in Fig. 8.

E_W increases in a parabolic shape as the monopiles penetrate into the seabed. The clear differences in E_W among the various monopiles can be found, in particular as the penetration depth increases. The cylindrical monopile, MP-C requires the largest energy to reach a given penetration depth, whilst the fully-tapered pile, MP-T requires the lowest. In essence, the change of cumulative driving energy provided from hammer impact should be consistent with that of the required hammer blow counts, as will be discussed later.

4.2. Dissipation process of driving energy

To identify the dissipation process of driving energy and capture the energy exchanges of hammer impact for the monopiles with various geometries, energy balance analyses involving the different energy terms for monopiles by impact driving into clays are carried out. The equation of energy balance can be written, at any time, as

$$E_{Balance} = E_I + E_F + E_V + E_K - E_W \tag{14}$$

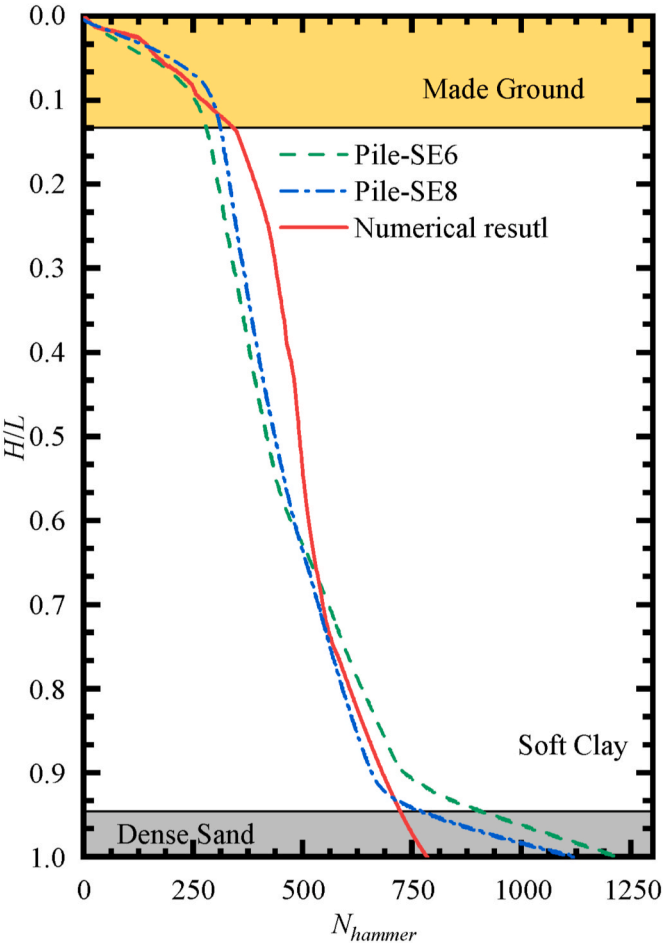

Fig. 7. Validation against field observations for Pile SE-6 and Pile SE-8.

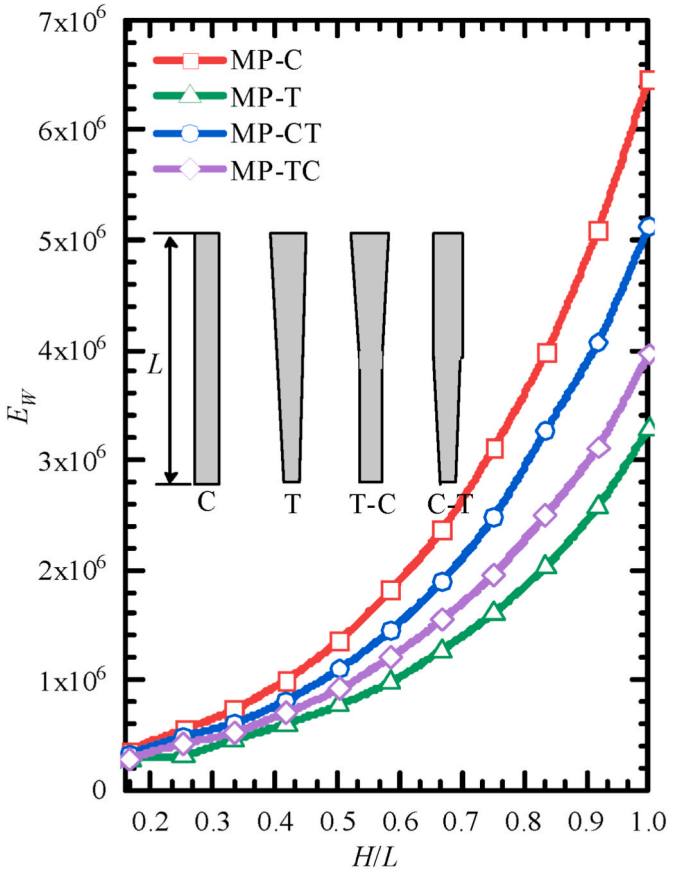

Fig. 8. Cumulative driving energy during the whole installation process for monopiles with various geometries.

where $E_{balance}$ is the total energy balance; E_I is the internal energy of the system; E_F is the energy dissipated by contact force between pile-soil interfaces; E_V is the energy dissipated by viscous effects of materials (soil viscosity and interface adhesion); E_K is kinetic energy transferred for pile impact driving and E_W is the total driving energy from hammer impact. More details of energy components in the system can be found in the Appendix. It needs to be emphasized that $E_{balance}$ could be only approximating a constant. The approximation is due to a fact that the recoverable strain energy (the term of components of internal energy) is computed by a modified trapezoidal rule in Abaqus/Explicit, rather than an exact trapezoidal rule. Such behavior is common in geometrically nonlinear problems, and one can only assess that the variation in $E_{balance}$ only has a slight fluctuation below and above zero in the system with exergy balance. It means that $E_{balance} \approx 0$ represents the energy balance of the system.

For comparison, the maximum cumulative driving energy of MP-C (denoted as E_{WC}) is used to normalize all the energy components in the systems of MP-T, MP-CT, and MP-TC. The energy dissipation process of various monopiles is shown in Fig. 9. It can be observed that all the traced $E_{balance}$ approximately iterates below or above zero, hence confirming the energy balance of the system in the whole installation process. During the installation process, the E_W delivered from hammer energy on the pile head is more readily transferred as E_I, which is composed of elastic, plastic and time-dependent strain energy of clays. The role of E_I in the monopile installation process can be displayed as the mobilization of soil resistance, as it is closely related to the elastic and plastic strain energy of soils. The other gradually-cumulative energy components transferred from E_W are E_V and E_F used for providing pile-soil interface contact force. Regarding the kinetic energy (E_K), direct use for driving piles, it is a variable with cyclic change linking closely with the penetration velocity of piles, and generated at the start and fully dissipated at the end of a hammer blow. Namely, the monopiles are at-rest when $E_K = 0$. Therefore, it can be initially observed in Fig. 9. For deeper penetration, as E_W accumulates and increases gradually, the

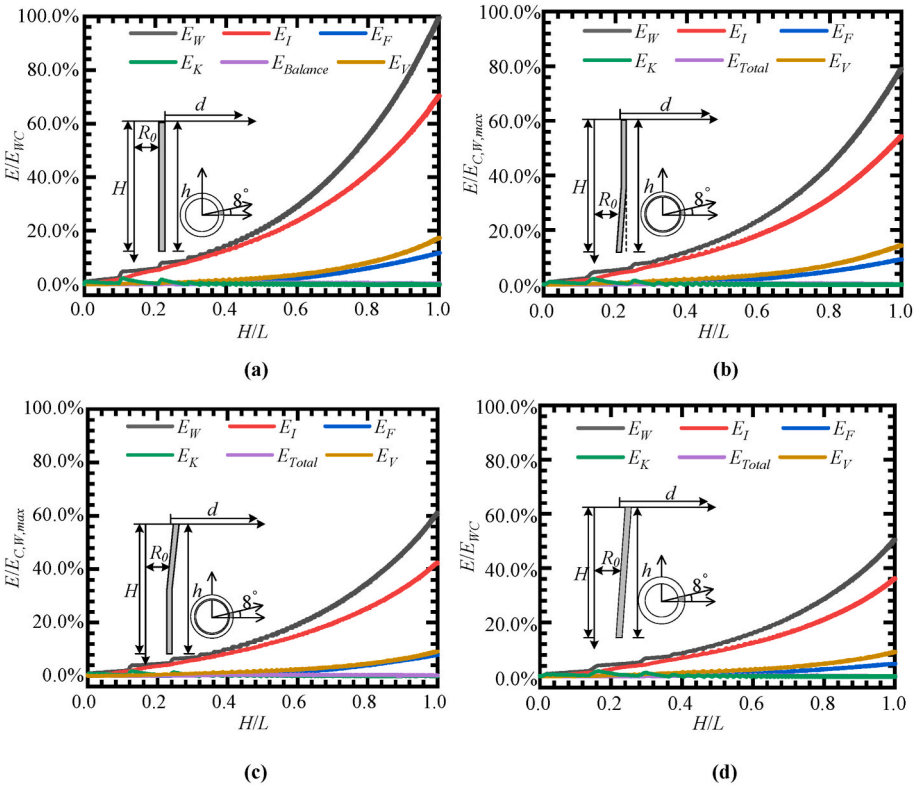

Fig. 9. Dissipation process of different energy terms during monopile driving: (a) MP-C; (b) MP-CT; (c) MP-TC and (d) MP-T.

value of E_K becomes very small relative to E_W.

The comparison indicates that the normalized values of E_W/E_{WC}, E_I/E_{WC}, E_V/E_{WC}, E_F/E_{WC} are the smallest for MP-T, followed by MP-TC, MP-CT, and MP-C. This highlights the benefits in the use of tapered monopiles. To quantify this benefit, taking MP-C as a benchmark, the comparisons of the different energy terms normalized by E_{WC} for various monopiles at the end of the installation are tabulated in Table 5. It can be seen that Pile-T dramatically reduces the required driving energy, in which the E_W of MP-T required is approximately half of the E_{WC}. From Table 5, we can also find that the internal energy in the system is where the most driving energy goes, and the sum of energy lost in the interface contact and soil viscosity is just about 30% for various pile types. It should be noted that the energy losses of 30% on interfaces may be somewhat underestimated as the energy losses from the water column, heat, and noise are neglected here. The realistic energy losses may be up to 40%. It can be, however, still concluded that for large-diameter monopiles with a diameter up to 10m in undrained clays, the hammer energy is more transferred to the soils around monopiles in a form of internal energy.

4.3. Energy exchanges during a hammer blow

The energy exchange during a hammer blow (i.e. a loading step with a duration of 0.2s) is studied in this section. The different energy terms during a hammer blow for various monopiles at $H = 0.5L$ and $H = L$ are given in Figs. 10 and 11, respectively. The rated output (maximum net energy) of the Hydrohammer® S-4000 is 4000 kJ. Note that, from these two figures, all the running results show the transferred energy traced on the pile head (cumulative driving energy) is slightly lower than the rated output of the hammer after 0.02s (impacting time of hammer). Such a difference is due to the discrepancies in the modeling details (the hammer and anvil impedances are not present in the ABAQUS model) (Vantomme et al., 2019).

During a hammer impact (0–0.02s), the cumulative driving energy E_W and the transferred kinetic energy E_K gradually increase to drive the monopiles, and the soil strength and interface contact are mobilized continually. Note that this process is not statically equilibrium from a viewpoint of force analysis. After 0.02s, the E_W is no longer increasing, hence E_K gradually dissipates to zero at around 0.1s which corresponds to the time that the monopile driving is suspended. At 0.10s, the system reaches static mechanical equilibrium. It is noted that, from 0.02 to 0.10s, the E_I, E_V, and E_F are still accumulated to resist pile driving. From 0.10 to 0.20s, all the energy terms remain constant and the hammer has been lifted for the next blow. Therefore, the energy exchanges of the system from 0.1–0.2s are not given in the figures.

The comparisons of energy terms among various monopiles during a hammer blow in Figs. 10 and 11 show that, under the same rated output of hammer, tapered monopiles have the larger kinetic energy E_K, indicating they have higher efficiency of energy transfer (E_K/E_W). In addition, the taper treatment reduces the energy dissipation of E_F due to the contact forces between pile-soil interfaces as tapering monopiles are beneficial to reducing the radial stresses on both the outside and the inside pile-soil interfaces (Tavasoli and Ghazavi, 2020). The values of E_I and E_V are approximate for various shapes' monopiles as they are mainly governed by material behaviors. The further comparison between Figs. 10 and 11 for the same monopile implies that E_K/E_W will reduce as monopile advances into deeper soils, as a result of gradually-increased penetration resistances. Therefore, it is always very difficult for penetration in the later installation, in practice.

Table 5
Comparisons of different energy terms for monopiles with various geometries.

MP-type	E_W/E_{WC}	E_I/E_{WC}	E_F/E_{WC}	E_V/E_{WC}	$E_I+E_F+E_V/E_{WC}$
C	100.00%	70.50%	11.70%	17.35%	99.55%
CT	79.13%	54.29%	9.20%	14.38%	77.87%
TC	61.26%	42.52%	7.84%	9.16%	59.52%
T	50.71%	36.30%	4.71%	9.13%	50.14%

5. Installation mechanisms

5.1. Hammer blow counts

Fig. 12(a) and (b) show the variations in hammer blow counts (N_{hammer}) and driving depth per blow (h_v) with normalized penetration depth (H/L) for monopile with various geometries (MP-C, MP-T, MP-TC and MP-CT), respectively. The self-weight penetration phase of large diameter monopiles for OWTs, where the self-weight is not smaller than penetration resistance, needs to be considered before the impact driving. However, limited by the computational cost (taking a very long time during self-weight penetration), we drove the pile using hammer impact at the beginning of the installation. As shown in Fig. 12(a) and (b), hammer blow counts increase with an increase in the penetration depth, following an inverted-parabolic curve, while penetration depth per blow gradually decreases in the shape of a parabola. This is because the penetration resistance (radial stress on the interface) gradually increases as the piling advances.

It can be also found from Fig. 12(a) that at very lower hammer blow counts, the monopiles are rapidly driven to a penetration depth around $0.3L$ that approximately corresponded to the expected self-weight penetration depth. The driving depth per blow h_v (corresponding to installation efficiency) is also comparatively high in this phase (Fig. 12 (b)). Such rapid penetration in the initial phase is due to the much larger driving impact force and very smaller penetration resistance that the pile is subjected to.

The comparisons of N of monopiles with various shapes indicate that MP-T has the smallest N_{hammer} value of 866, followed by MP-TC (N_{hammer} = 1031), MP-CT (N_{hammer} = 1036), and MP-C (N_{hammer} = 1661). This change law of hammer blow counts is similar to that of cumulative driving energy (Fig. 8). The hammer blow counts of MP-C required are approximately twice that of MP-T. It shows that for the same material volume and penetration depth, the taper treatment (tapered/semi-tapered piles) can remarkably reduce the hammer blow counts. This phenomenon is resulted from that the inclined tapered angle reducing the normal and shear stiffness of monopiles' base and shaft (Tavasoli and Ghazavi, 2020). This demonstrates the feasibility of tapered/semi-tapered monopiles. It is of interest that this so-called optimized effect is gradually weakened as the penetration depth increases (Fig. 12(b)), in particular, $H/L > 0.8$ since the required driving force is very large.

5.2. Penetration resistances

The drivability performances can be more clearly characterized by distributions of penetration resistances of piles. Fig. 13 depicts the distributions of skin resistance F_s and total penetration resistance F_t with normalized penetration depth (H/L) during the impact driving for large diameter monopiles of various shapes. The base resistance (i.e. end-bearing resistance, F_b) can be thus obtained using $F_t - F_s$ (i.e. horizontal spacing between the envelopes). All the resistances extracted from numerical models are normalized by the maximum instantaneous impact driving force (f_{max}) for comparison. The same inputted load-time curve is defined to ensure the loading frequencies of monopiles of various shapes. Fig. 13 observes some interesting phenomena as follows: (1) The smaller number of cycles per depth can be found for tapered monopile MP-T, MP-TC, and MP-CT owing to the less N_{hammer} required. Similarly, for four large-diameter monopiles studied, all the required N_{hammer} are very small in the self-weight penetration phase, resulting in a very small number of cycles per depth at the installation beginning. (2) The amplitudes of resistances are closely relevant to monopiles' geometries. It is observed that MP-T has the smallest amplitude representing the lowest penetration resistances provided by foundation soils. (3) The

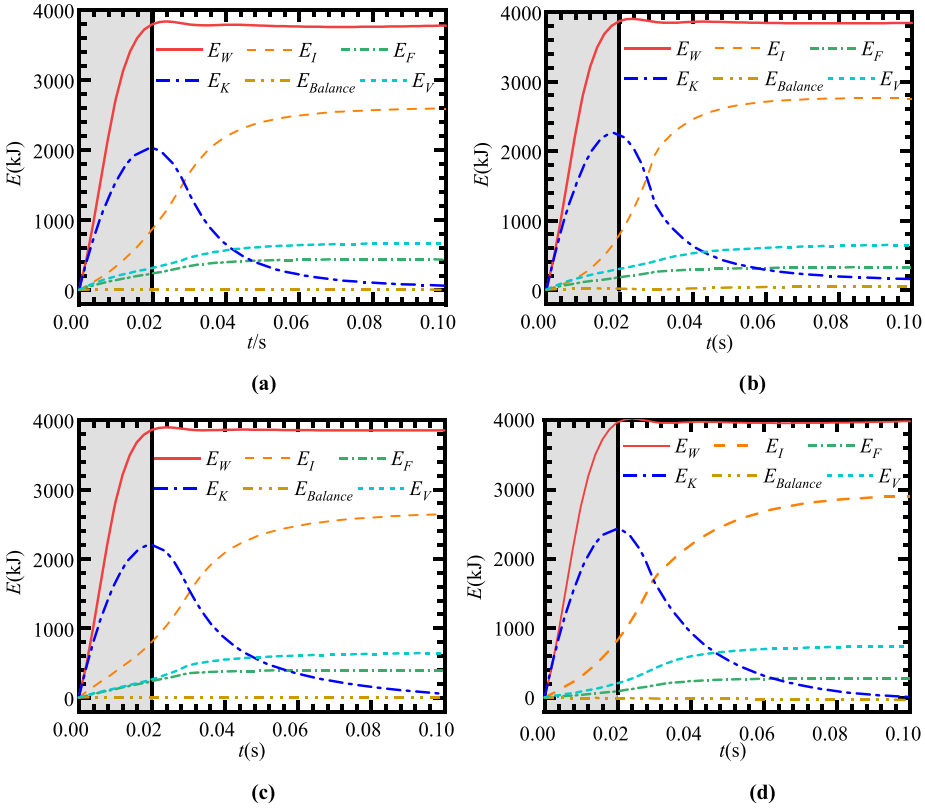

Fig. 10. Energy exchanges of different energy terms during a hammer blow at $H/L = 0.5$: (a) MP-C; (b) MP-CT; (c) MP-TC and (d) MP-T.

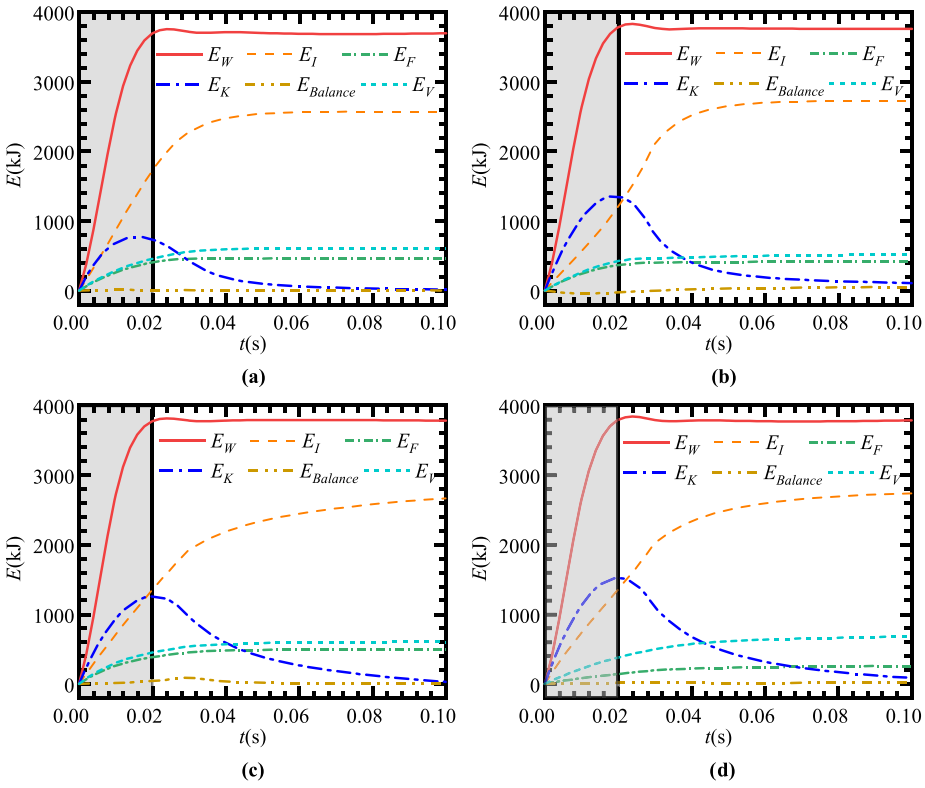

Fig. 11. Energy exchanges of different energy terms during a hammer blow at $H/L = 1.0$: (a) MP-C; (b) MP-CT; (c) MP-TC and (d) MP-T.

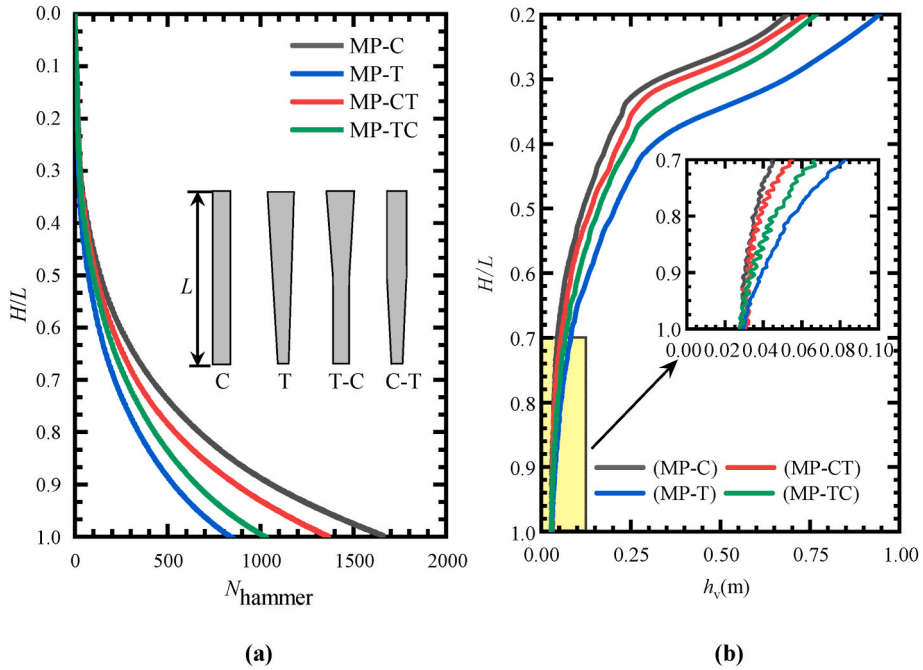

Fig. 12. Drivability performance of large diameter monopiles with various geometries: (a) hammer blow counts and (b) penetration depth per blow.

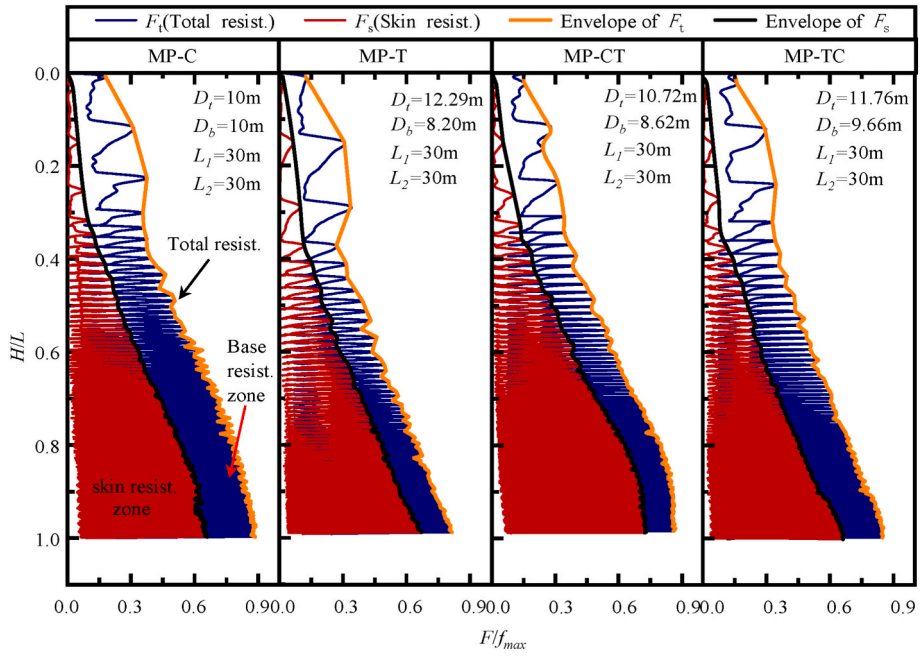

Fig. 13. Variations in total penetration resistance and skin resistance with penetration depth for monopiles with various geometries.

differences among total penetration resistances at $H/L = 1$ for various monopiles are relatively smaller, with $F_t/f_{max} \approx 0.9$ in this study. This explains why the penetration depth per blow $h_v \approx 0.03$ m at $H/L = 1$ for various monopiles (Fig. 12(b)).

The skin resistance differences between the outside and the inside for four monopiles of various geometric shapes are given in Fig. 14. As seen, we can roughly capture the self-weight penetration depth of various monopiles, corresponding to the smaller skin resistance and cycle number per depth, denoted as *Phase I*. Here we can also find that the self-weight penetration depths are 0.29*L* for MP-C, 0.31*L* for MP-TC, 0.34 *L* for MP-CT, and 0.35 *L* for MP-T, respectively. This shows that the tapering pile is beneficial for increasing the self-weight penetration depth of monopiles.

It can be also found from Fig. 14 that the skin resistance difference between on the outside and the inside is very small for MP-C, implying that the role of the soil plugging effect inside super-large-diameter monopiles ($D_{in} = 10$ m) on the skin resistance is very small. It is of interest that the impact driving process of such cylindrical monopiles does not appear to cause the additional degradation of inside skin resistance, which is unlike that for small-to-medium diameter monopiles. The relatively obvious differences between tapered and semi-tapered monopiles are attributed to that the taper angle increases the normal pressure on the monopile shaft. This can be explained by the fact that, for MP-T and MP-CT, the use of taper increases the outside skin

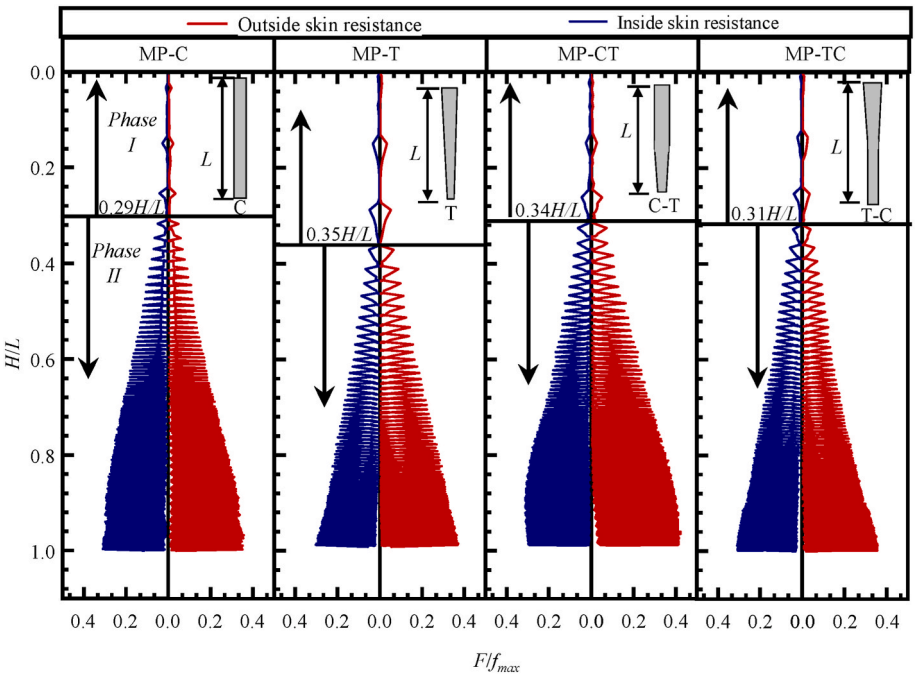

Fig. 14. Differences between outside and inside skin resistances with penetration depth for monopiles with various geometries.

resistance as the outside pile-soil interface with the tapered section would be additionally subjected to radial expansion resistance. Moreover, both the increments of the outside and the inside skin resistances gradually decrease with the increase of penetration depth since the seismic shear strength of clays is weakened as the cycle number increases.

It should be noted that the friction fatigue problem of pile-soil interfaces induced by cyclic loading is not modeled here as the CEL approach implemented into Abaqus/Explicit does not allow the user-defined contact models to modify the calculation of contact forces (Daryaei et al., 2020; Staubach et al., 2021). From Fig. 14, for a tapered pile with a lower tapered angle (e.g. 2 deg), the influence of neglecting friction fatigue on the differences of skin resistances on the inside and outside should be limited. However, it is not the case if tapering the pile

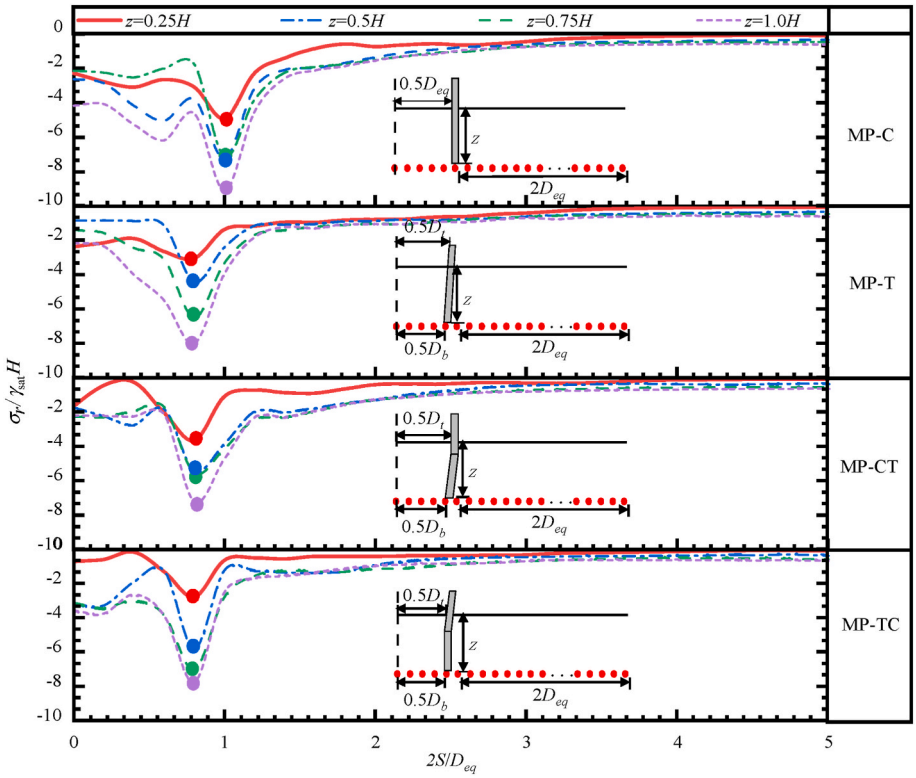

Fig. 15. Variations in the normalized radial stress around the base of monopiles with various geometries along with the normalized radial distance at various penetration depths.

with a larger angle. In this case, neglecting the friction fatigue may significantly influence the magnitude of skin resistances, which would be more pronounced for cylindrical pile as it is subjected to larger radial stress than tapered piles. Therefore, more numerical works are required in the future for such purposes.

5.3. Radial stresses

The equivalent diameter (D_{eq}) of monopiles, obtained using the pile material volume divided by pile depth, is introduced to normalize the radial distance to axis of symmetry (S). The D_{eq} obtained is 10.0m in this study. Fig. 15 shows the variations in the radial stresses $\sigma_r/\gamma_{sat}H$ around the base of monopiles with various geometric shapes along the normalized radial distance S/D_{eq} at various penetration depths (z_s/H = 0.25, 0.50, 0.75, 1.00), respectively. It follows from Fig. 15 that the radial stresses inside and outside the shaft increase with advancing the monopiles due to the gradual increase in downforce, the maximum radial stresses are located on the monopile toe due to the stress concentration. The observed distribution of $\sigma_r/\gamma_{sat}H$ around the base follows the inverted-parabolic curve. Interestingly, the radial stress of clays inside the large-diameter monopile does not show the effect of rapidly increasing due to the so-called soil plugging effect (Ko et al., 2016). This means that the soil plugging effect for such large diameter monopiles (D_{in} > 10 m) might be neglected in design, at least in clays. The comparison among various monopiles gives that the maximum radial stresses (solid points in the figure) at each penetration stage for MP-T, MP-CT, and MP-TC are lower than that for MP-C, highlighting the superiority of taper treatment used in OWT monopiles.

Fig. 16 describes the variations in the radial stresses $\sigma_r/\gamma_{sat}H$ around the shaft of monopiles with various geometric shapes along with soil buried depth at various penetration depths (H/L = 0.25, 0.50, 0.75, 1.00), respectively. Pile driving is a process of cavity expansion, leading to an stress concentration around pile toes. Therefore, the radial stresses of clays around the pile toe rapidly increase (Fig. 16). This phenomenon is more significant as advancing monopiles, therefore, the maximum radial stresses (solid points in the figure) also increase gradually. The distribution of radial stress along the monopile shafts shows a convex curve. In addition, the effect of stress relaxation in clays can be found far from pile toe, compared to the $K_0\gamma_{sat}H$ stress line. The comparisons of induced maximum radial stress around the pile toe also highlight the advantage of tapered/semi-tapered monopiles, as emphasized above.

It can be further seen from Fig. 16 that for MP-T and MP-CT of which the upper section has a larger diameter, radial expansion resistance will be enhanced such that the larger outside skin resistance is generated, compared to that of MP-C. The tapered monopile base with a smaller diameter behaves oppositely. In all, Fig. 16 comprehensively shows that tapered piles would not experience much greater radial stress than a straight pile.

To assess the risk of pile buckling, the differences between the inside and outside skin resistances when the various monopiles are driven at designed depth are highlighted in Fig. 17. It demonstrates that the contact force on the inside of tapered piles is slightly lower than that on the outside. This would be more pronounced for MP-T and MP-CT of which the upper section has a larger diameter. It follows that tapering monopiles may increase the risk of propagation buckling in pile imperfections as it will obtain better driving performance. As such, the emphasis of future works also should be placed on the optimization of taper angle for tapered piles used in the offshore industry.

6. Limitation

Limited by computational costs and inherent flaws of the CEL technique, it is currently difficult to fully realistically model the dynamic installation process of monopiles. For example, in offshore engineering, the modeling of seawater is of significance for the interpretation of installation mechanisms. The water column would lead to some energy losses. The simulation of noise and heat produced in the installation process was also hindered by the unattainable use of acoustics and heat elements. The cyclic loading-enabled friction fatigue is unable to be stimulated due to the inability to implement an interface subroutine in the CEL approach. In addition, the assumption of a rigid body means a hammer blow must mobilize the full mass of the pile at the same time, rather than progressively as the force wave moves down the pile. In other words, the use of a rigid body may provide too optimistic results, e.g., underestimating skin resistance and hammer blow count. Therefore, doing a robust design through numerical analysis may require the assumption of an elastic body made. In the opinion of the authors, the use of deformable finite elements may yield strongly oscillating results under a high impacting force (numerical instability). These may be one

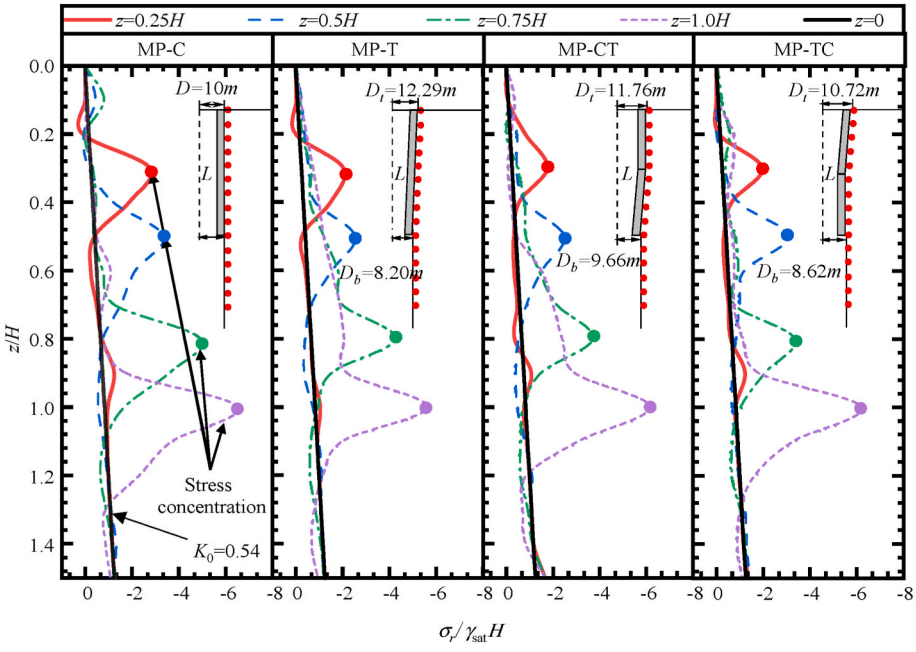

Fig. 16. Variations in the normalized radial stress around the shaft of monopiles with various geometries along with soil buried depth at various penetration depths.

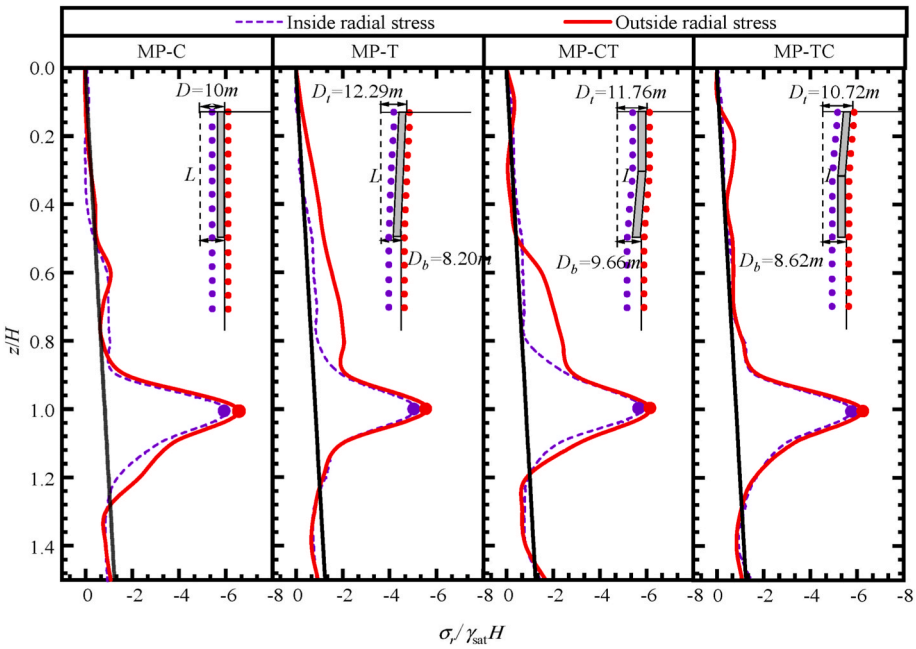

Fig. 17. Comparison of inside and outside radial stresses around the shafts of monopiles with various geometries at designed depth.

of the obstacles that explain the research paucity regarding the energy balance analyses of large diameter piles driven by hammer impact and quantitatively predicting skin resistance of pile-soil interface. These drawbacks should be addressed in the follow-up research.

7. Conclusions and discussion

This numerical work described in this paper investigated the temporal evolution of the energy balance during the installation process of large diameter tapered monopiles, and studied the associated installation mechanisms. An important aim of the paper was to explore the potential use of tapered piles in offshore engineering. The widely-used installation method of impact driving using a hydraulic hammer was chosen to drive the monopiles. A 3D-LDFE model using the CEL approach was established to simulate impact driving of tapered and semi-tapered monopiles with various geometries (MP-C, MP-T, MP-TC, MP-CT). The seabed soil was considered as undrained kaolin clay, which was simulated by an advanced user-defined HC model. The hammer blow was characterized in the numerical model as a force-time curve defined by the operating data of a state-of-the-art Hydrohammer® S-4000. The whole installation process of various monopiles was simulated. The developed model was validated by field tests with reasonably good agreement. The main findings of this work can be noted as follows:

1. Tapering piles can enhance the driving performance with less driving energy and a higher energy transfer rate. MP-T is proven to have the most remarkable optimized effect on the installation, followed by MP-CT, MP-TC, and MP-C. The feasibility of tapered large-diameter monopiles supporting OWTs is demonstrated.
2. Around the energy losses of 30% to interface for large-diameter monopiles with a diameter up to 10m in undrained soft clays can be documented, the hammer energy may be more transferred to the ground in a form of internal energy. The kinetic energy transferred from hammer energy during a hammer blow is gradually reduced as monopile advances into deeper soils, corresponding to the change of penetration velocity.
3. The use of taper is beneficial to reduce the penetration resistances from the outside and the inside pile-soil interface but the outside one with a tapered section would be additionally subjected to radial expansion resistance. Therefore, tapering monopiles may somehow increase the risk of propagation buckling in pile imperfections.
4. During the impact driving, the hammer blow counts increase in the shape of an inverted parabola as advancing monopiles, and the associated penetration depth per blow gradually decreases, following a parabolic curve. The frequency of hammer impacting is higher and higher as the installation progresses, being subjected to larger and larger penetration resistances. The soil plugging effect on the installation of such super-larger-diameter monopiles ($D_{in} \geq 10$ m) is almost negligible.

Although tapered monopiles have shown great superiority for reducing penetration resistance, some practical factors have to be highlighted. Since the maximum bending moment occurs near the mudline such that a larger top diameter generates high wave loading, the structural benefits would be weakened for the cases of MP-T and MP-TC. As a result, MP-CT may be more practical, making a compromise between installation efficiency and working performance.

The studied installation mechanisms and energy balance analyses provide a theoretical guideline for the future use of tapered monopiles in offshore engineering. However, limited by article length, some referable indicators to interpret the installation mechanisms, e.g., plastic zone, soil deformation, and displacement, as well as deformed soil flow are not given here, which will be discussed in subsequent research.

CRediT authorship contribution statement

Fuquan Chen: Writing – review & editing, Conceptualization, Methodology, Supervision, Funding acquisition. **Liyang Liu:** Software, Data curation. **Fengwen Lai:** Writing – original draft, Writing – review & editing, Supervision, Formal analysis. **Kenneth Gavin:** Writing – review & editing, Supervision. **Kevin N. Flynn:** Writing – review & editing, Validation. **Yida Li:** Writing – original draft, Software, Data curation.

Declaration of competing interest

The authors declare that they have no known competing financial interests or personal relationships that could have appeared to influence the work reported in this paper.

Data availability

Data will be made available on request.

Acknowledgments

This study is financially supported by the National Natural Science Foundation of China (Grant No. 42177121). The corresponding author is supported by a CSC grant. The permission of AGL consulting to publish monitoring data of pile installation Tilbury, UK is greatly acknowledged. The corresponding author finally would like to appreciate invaluable suggestions and discussion on the use of Hypoplasticity Clay model from Dr. Patrick Staubach at Ruhr-Universität Bochum, Germany.

Appendix. Energy components in the system

Dynamic piling is an energy-dissipating process where the soil assembly transits in between two equilibrium [from the at-rest position before hammer release (at time $t = 0$) to the at-rest position after penetration ends (at time $t = t_{total}$). In this installation process, energy exchange and dissipation occur in the system. All related energy terms can be traced during each computation step (a loading cycle). For energy balance analysis, it is clearer for the equation establishment of energy balance to consider separately three sub-systems: the driven monopiles and the clays as well as the pile-soil interfaces.

The energy balance can be written as

$$E_{\text{Balance}} = E_I + E_F + E_V + E_K - E_w \tag{A. 1}$$

where the definition of each energy term has been given above and will be again highlighted below.

The monopile is assumed as rigidity and, hence, the driving energy E_{wi} delivered by hammer impact on the pile head can be theoretically computed for each blow with loading duration of t_i by integrating the total driving load multiplied by the simulated monopile velocity history $\dot{\boldsymbol{x}}_{pile}$:

$$E_{W_i} = \int_0^{t_i} F_c(t)\dot{\boldsymbol{x}}_{pile}(t)dt \tag{A. 2}$$

The cumulative driving energy in the installation process can be summed over the whole driving process:

$$E_W = \sum_{i=1}^{N_{hammer}} E_{W_i} \tag{A. 3}$$

E_K is the instantaneous kinetic energy of the pile-soil system, which can be determined by taking into account the velocities of monopile and soils:

$$E_K = \frac{1}{2}\left[\boldsymbol{m}_{pile}\boldsymbol{v}_{pile}^2(t) + \boldsymbol{m}_{soil}\boldsymbol{x}_{soil}^2(t)\right] \tag{A. 4}$$

where $\dot{\boldsymbol{x}}_{soil}$ is the relative velocity of soil particles; $\boldsymbol{m}_{pile}$ and $\boldsymbol{m}_{soil}$ are the mass density of monopile and soil particles, respectively. Due to the smaller velocities and masses of soil particles, the kinetic energy of the system is governed by monopiles.

The energy dissipated by contact stress $\boldsymbol{\sigma}^f$ between the contact surfaces can be expressed as

$$E_F = \int_0^t \left(\int_V \boldsymbol{\sigma}^f : \boldsymbol{\varepsilon}^f dV\right)dt \tag{A. 5}$$

where $\boldsymbol{\sigma}^f$ is the interface adhesion under undrained conditions, $\boldsymbol{\varepsilon}^f$ is the relative strain rate between pile body and soil particles around, and V denotes a volume occupied by a part of the body (soil or interface) in the current configuration.

The energy dissipated by viscous effects (E_V) can be generated from material viscosity, material damping (soils and interfaces), and dashpots, respectively. The E_V can be determined using

$$E_V = \int_0^{t_{total}} \left(\int_V \boldsymbol{\sigma}^v : \dot{\boldsymbol{\varepsilon}} dV\right)dt \tag{A. 6}$$

where $\boldsymbol{\sigma}^v$ is the viscous stresses defined for bulk viscosity, material damping, and dashpots, which could be occurred in soils and pile-soil interfaces; $\dot{\boldsymbol{\varepsilon}}$ is a concept of composited strain rate and $\dot{\boldsymbol{\varepsilon}} = \dot{\boldsymbol{\varepsilon}}^{el} + \dot{\boldsymbol{\varepsilon}}^{pl} + \dot{\boldsymbol{\varepsilon}}^{er}$ ($\dot{\boldsymbol{\varepsilon}}^{el}$, $\dot{\boldsymbol{\varepsilon}}^{pl}$ and $\dot{\boldsymbol{\varepsilon}}^{er}$ are elastic, plastic, and creep strain rates, respectively).

The internal energy (i.e. remaining energy) can be considered as mainly generated by the strain energy of soils involving elastic, plastic and creep strain of material under stresses $\boldsymbol{\sigma}^c$ derived from constitutive equations, without viscous dissipation effects included. Therefore, we have

$$\begin{aligned} E_I &= \int_0^{t_{total}} \left[\int_V \boldsymbol{\sigma}^c : \dot{\boldsymbol{\varepsilon}} dV\right]dt \\ &= \int_0^t \left(\int_V \boldsymbol{\sigma}^c : \dot{\boldsymbol{\varepsilon}}^{el} dV\right)dt + \int_0^t \left(\int_V \boldsymbol{\sigma}^c : \dot{\boldsymbol{\varepsilon}}^{pl} dV\right)dt + \int_0^t \left(\int_V \boldsymbol{\sigma}^c : \dot{\boldsymbol{\varepsilon}}^{er} dV\right)dt \\ &= E_S + E_P + E_C \end{aligned} \tag{A. 7}$$

where E_S, E_P and E_C are the applied elastic strain energy, the energy dissipated by plasticity, and the energy dissipated by time-dependent deformation (creep, swelling, and viscoelasticity), respectively. Since this study focuses on the remaining energy transferred to the ground, the energy terms are not split off in the main text.

Appendix A. Supplementary data

Supplementary data to this article can be found online at https://doi.org/10.1016/j.oceaneng.2022.113017.

References

ASTM-A252, 2010. Standard Specification for Welded and Seamless Steel Pipe Piles, Edition. ASTM International, West Conshohocken,PA,USA.

Byrne, B.W., Houlsby, G.T., Burd, H.J., Gavin, K.G., Igoe, D.J.P., Jardine, R.J., Martin, C. M., McAdam, R.A., Potts, D.M., Taborda, D.M.G., Zdravkovic, L., 2020a. PISA design model for monopiles for offshore wind turbines: application to a stiff glacial clay till. Geotechnique 70 (11), 1030–1047.

Byrne, B.W., McAdam, R.A., Burd, H.J., Beuckelaers, W.J.A.P., Gavin, K.G., Houlsby, G. T., Igoe, D.J.P., Jardine, R.J., Martin, C.M., Wood, A.M., Potts, D.M., Gretlund, J.S., Taborda, D.M.G., Zdravkovic, L., 2020b. Monotonic laterally loaded pile testing in a stiff glacial clay till at Cowden. Geotechnique 70 (11), 970–985.

Charlton, T., Rouainia, M., 2020. Cyclic performance of a monopile in spatially variable clay using an advanced constitutive model. Soil Dynam. Earthq. Eng. 140 (2021), 106437.

Chortis, G., Askarinejad, A., Prendergast, L.J., Li, Q., Gavin, K., 2020. Influence of scour depth and type on p-y curves for monopiles in sand under monotonic lateral loading in a geotechnical centrifuge. Ocean. Eng. 197 (2020), 106838.

Daryaei, R., Bakroon, M., Aubram, D., Rackwitz, F., 2020. Numerical evaluation of the soil behavior during pipe-pile installation using impact and vibratory driving in sand. Soil Dynam. Earthq. Eng. 134 (2020), 106177.

Ekanayake, S.D., Liyanapathirana, D.S., Leo, C.J., 2013. Influence zone around a closed-ended pile during vibratory driving. Soil Dynam. Earthq. Eng. 53 (2013), 26–36.

El Naggar, M.H., Wei, J.Q., 1999. Response of tapered piles subjected to lateral loading. Can. Geotech. J. 36 (1), 52–71.

Fan, S., Bienen, B., Randolph, M.F., 2021. Effects of monopile installation on subsequent lateral response in sand. I: pile installation. J. Geotech. Geoenviron. Eng. 147 (5), 04021021.

Flynn, K.N., McCabe, B.A., 2019. Driven cast-in-situ piles installed using hydraulic hammers: installation energy transfer and driveability assessment. Soils Found. 59 (6), 1946–1959.

Gavin, K., Kovacevic, M.S., Igoe, D., 2021. A review of CPT based axial pile design in The Netherlands. Undergr. Space 6 (1), 85–99.

Ghazavi, M., Tavasoli, O.J.S.D., Engineering, E., 2012. Character. Non Uniform. Cross Section. Drivability. 43 (2012), 287–299.

Harireche, O., Naqash, M.T., Farooq, Q.U., 2021. A full numerical model for the installation analysis of suction caissons in sand. Ocean. Eng. 234 (2021), 109173.

Kadlicek, T., Masin, D., 2020. The strength reduction method in clay hypoplasticity. Comput. Geotech. 126 (2020), 103687.

Ko, J., Jeong, S., Lee, J.K., 2016. Large deformation FE analysis of driven steel pipe piles with soil plugging. Comput. Geotech. 71 (2016), 82–97.

Kodikara, J., Kong, K.H., Haque, A., 2006. Numerical evaluation of side resistance of tapered piles in mudstone. Geotechnique 56 (7), 505–510.

Kodikara, J.K., Moore, I.D., 1993. Axial response of tapered piles in cohesive frictional ground. J. Geotechn. Eng. ASCE. 119 (4), 675–693.

Kurian, N.P., Srinivas, M.S., 1995. Studies on the behaviour of axially loaded tapered piles by the finite element method. Int. J. Numer. Anal. Methods GeoMech. 19 (12), 869–888.

Lai, F., Liu, S., Li, Y., Sun, Y., 2022a. A new installation technology of large diameter deeply-buried caissons: practical application and observed performance. Tunn. Undergr. Space Technol. 125 (2022), 104507.

Lai, F., Liu, S., Deng, Y., Sun, Y., Wu, K., Liu, H., 2020. Numerical investigations of the installation process of giant deep-buried circular open caissons in undrained clay. Comput. Geotech. 118 (2020), 103322.

Lai, F., Zhang, N., Liu, S., Sun, Y., Li, Y., 2021. Ground movements induced by installation of twin large diameter deeply-buried caissons: 3D numerical modeling. Acta Geotechnica 16 (9), 2933–2961.

Lai, F., Zhang, N., Liu, S., Yang, D., 2022b. A generalised analytical framework for active earth pressure on retaining walls with narrow soil. Geotechnique 1–16. https://doi.org/10.1680/jgeot.21.00305.

Li, L.C., Wu, W.B., Liu, H., Lehane, B., 2021. DEM analysis of the plugging effect of open-ended pile during the installation process. Ocean. Eng. 220 (2021), 108375.

Li, Y.P., Yi, J.T., Lee, F.H., Goh, S.H., Hu, J., 2018. Effect of lattice leg and sleeve on the transient vertical bearing capacity of deeply penetrated spudcans in clay. J. Geotech. Geoenviron. Eng. 144 (5), 04018019.

Lunne, T., Powell, J.J., Robertson, P.K., 2002. Cone Penetration Testing in Geotechnical Practice. CRC Press, London.

Masin, D., 2014. Clay hypoplasticity model including stiffness anisotropy. Geotechnique 64 (3), 232–238.

Mašín, D., 2019. Modelling of Soil Behaviour with Hypoplasticity. Springer Cham, Switzerland AG.

Pucker, T., Grabe, J., 2012. Numerical simulation of the installation process of full displacement piles. Comput. Geotech. 45 (2012), 93–106.

Rausche, F., Klesney, 2007. Hammer types, efficiencies and models in GRLWEAP. In: PDCA 11th Annual International Conference and Exposition. Nashville, USA, pp. 97–118.

Sakr, M., El Naggar, M.H., 2003. Centrifuge modeling of tapered piles in sand. Geotech. Test J. 26 (1), 22–35.

Skempton, A., 1953. The Post-glacial Clays of Thames Estuary at Tilbury and Shell-Haven. 3rd ICSMFE, Proc, pp. 302–308.

Soleimani, M., Weienfels, C., 2021. Numerical simulation of pile installations in a hypoplastic framework using an SPH based method. Comput. Geotech. 133 (2021), 104006.

Sormeie, A., Ghazavi, M., 2018. Analysis of non-uniform piles driven into cohesive soils. Soil Dynam. Earthq. Eng. 109 (2018), 282–285.

Staubach, P., Machaček, J., Skowronek, J., Wichtmann, T., 2021. Vibratory pile driving in water-saturated sand: back-analysis of model tests using a hydro-mechanically coupled CEL method. Soils Found. 61 (1), 144–159.

Stutz, H., Masin, D., Sattari, A.S., Wuttke, F., 2017. A general approach to model interfaces using existing soil constitutive models application to hypoplasticity. Comput. Geotech. 87 (2017), 115–127.

Sunday, K., Brennan, F., 2021. A review of offshore wind monopiles structural design achievements and challenges. Ocean. Eng. 235 (2021), 109409.

Tavasoli, O., Ghazavi, M., 2018. Wave propagation and ground vibrations due to non-uniform cross-sections piles driving. Comput. Geotech. 104 (2018), 13–21.

Tavasoli, O., Ghazavi, M., 2019. Driving behavior of stepped and tapered offshore piles due to hammer blows. Mar. Georesour. Geotechnol. 38 (6), 633–646.

Tavasoli, O., Ghazavi, M., 2020. Effect of tapered and semi-tapered geometry on the offshore piles driving performance. Ocean. Eng. 201 (2020), 107147.

Vantomme, F., Versteele, H., Cathie, D., 2019. Driving energy losses for constant diameter and tapered submerged monopiles. Appl. Ocean Res. 82 (2019), 337–345.

Wang, T., Liu, W.L., Wu, X.N., 2019. One-dimensional modelling of pile jacking installation based on CPT tests in sand. Geotechnique 69 (10), 877–887.

Wang, T., Zhang, Y., Bao, X.X., Wu, X.N., 2020. Mechanisms of soil plug formation of open-ended jacked pipe pile in clay. Comput. Geotech. 118 (2020), 103334.

Zdravkovic, L., Taborda, D.M.G., Potts, D.M., Abadias, D., Burd, H.J., Byrne, B.W., Gavin, K.G., Houlsby, G.T., Jardine, R.J., Martin, C.M., McAdam, R.A., Ushev, E., 2020. Finite-element modelling of laterally loaded piles in a stiff glacial clay till at Cowden. Geotechnique 70 (11), 999–1013.